Investigations and Corrections of the Light Output Uniformity of CsI(Tl) Crystals

M.-J. van Goethem[a], M.S. Wallace[a], B.E. Nett[a], M.A. Famiano[a†], K.R. Herner[a], D.J. Oostdyk[a], M.Mocko[a], W.G. Lynch[a], M.B. Tsang[a], P. Schotanus[b], J. Telfer[c], H.L. Clark[d], A. Moroni[e], R. de Souza[f], and L.G. Sobotka[g], [a]*National Superconducting Cyclotron Laboratory and Department of Physics and Astronomy, Michigan State University, East Lansing MI. 48824-1321,* [b]*Scionix, P.O. Box 143 3980 CC Bunnik, The Netherlands,*[c]*Thermo Hilger Crystals, Westwood, Margate, Kent, CT9 4JL, England,* [d]*Cyclotron Institute, Texas A&M University, College Station, Texas 77840,* [e]*Dipartimento di Fisica and INFN, I-20133 Milano, Italy,* [f]*Department of Chemistry and IUCF, Indiana University, Bloomington, Indiana 47405,* [g]*Department of Chemistry, Washington University, St. Louis, Missouri 63130.*

Abstract:

The dependencies of the light output response of CsI(Tl) crystals for various charged particle beams are investigated. Measurements were performed using 5.5 MeV ^{241}Am alpha particles, 220 MeV alpha and 110 MeV deuteron beams from the K500 Cyclotron at Texas A&M University, and p, ^{2}H, ^{3}He, ^{6}Li, and ^{7}Be beams from the Coupled Cyclotron Facility at Michigan State University. These measurements reveal a clear correlation between the non-uniformities observed in the same crystal for the various beams. Particle dependent global corrections were applied, resulting in final light output uniformities of the order of 0.1%. Annealed and non-annealed CsI(Tl) detectors and crystals with different thalium dopings are compared to determine whether annealing reduces the local variations in the light output. No significant correlation with the crystal fabrication process is observed.

PACS: 29.40.Mc; 29.90.+r

Keywords: Scintillators – light output; CsI(Tl) detectors; Scintillator non-uniformity; Resolution

[†]Corresponding Author: National Superconducting Cyclotron Laboratory, 164 South Shaw Lane, Michigan State University, East Lansing, MI 48824-1321. Tel: 517-333-6427. FAX: 517-353-5967. e-Mail: famiano@nscl.msu.edu

Introduction

Scintillators fabricated from thalium doped CsI (Cesium-Iodide) crystals have been extensively used for the detection of energetic charged particles [1-6]. This wide spread use stems from the facts that CsI(Tl) crystals can be readily machined, perform satisfactorily at room temperature, are not as hygroscopic as Na(Tl) crystals, and produce light with a spectrum that is well suited for readout via silicon photodiodes [1,3,5].

While excellent resolution is achievable for highly uniform crystals, the resolutions of actual crystals are negatively impacted by local and global non-uniformities in the light output of the crystal [1,4,5]. Variations in the light output of the order of 0.5% have been observed between ionization trajectories through the crystal that are separated by as little as 3mm [5]. These observations suggested that gains in resolution would be achieved if such local light output variations could be controlled [5].

Light output variations within scintillators have been explored in a variety of contexts because they are important for many scintillator applications. The corrections for light output variations vary from application to application, however. When scintillators are used for energetic γ-ray detection [7] or within large-scale sampling calorimeters [8], large volumes of these scintillators of the order of 10^2-10^4 cm^3 can be excited by a cascade of particles produced by the interaction of the incident particle with the scintillator. In such cases, the resolution is influenced by light output variations over distances of the order of centimeters, by statistics and by the degree to which the produced particles are confined to the scintillator volume. In contrast, charged particles with energies of 20-150 MeV/nucleon activate comparatively small volumes along their

trajectories in the crystal characterized by transverse dimensions of the order of millimeters; the major deposition occurs near the end of each trajectory where the stopping power attains maximum values characteristic of the Bragg peak. For such particles, the cascade of ionized electrons remains within the detector, the statistical accuracy can be very high; however, the light output uniformity over much smaller lateral dimensions of order of millimeters becomes critical. If a high degree of uniformity can be achieved or if the non-uniformity can be well characterized and the trajectory of each track defined by another tracking detector, the energy resolution can be remarkable. To achieve such resolutions, however, it is important to control or characterize the light output uniformity and to understand how it depends on the charge or mass of the incident particle. Only then can the potential resolution of such devices by realized.

The current investigation was motivated by the resolution requirements of the High Resolution Array (HiRA) for breakup spectroscopy experiments, in which energetic decay products of an excited nucleus are stopped in the CsI(Tl) crystals and the excitation energy of the nucleus is reconstructed from the final observables. The HiRA device consists of 20 telescopes; each telescope is composed of two silicon-strip detectors of 65μm and 1500μm thickness, backed by four CsI(Tl) crystals. The strips provide tracking information by dividing the 6.4x6.4 cm^2 active area of the silicon detectors into 1024 (32x32) square pixels, and accordingly, the 3.2x3.2 cm^2 active area of each CsI(Tl) crystal into 256 pixels. The beam direction and the pixel position define the trajectory of a particle. In all cases, the beam divergence was less than 20mrad, which contributes an uncertainty to the position of the beam particle trajectory at the end of a CsI(Tl) crystal that less than 800 μm, negligible compared to the pixel width of 3.2 mm. This

subdivision enables the non-uniformity of the CsI(Tl) light output to be modeled with precision and later corrected in the data analyses.

To investigate how the optimum resolution might be obtained, initial tests with eight test crystals and later tests with four final HiRA crystals were undertaken. We describe the preparation of these crystals, their physical properties and results obtained with an alpha source and a variety of energetic beams. Then we examine the systematic trends in the observed non-uniformities and how these trends can be precisely corrected via data analyses.

Methods

Discrete grids in the xy coordinate plane are mapped onto the scintillation crystals. At the coordinate x=i, y=j, the non-uniformity S_{ij} of light output for scintillation crystals is expressed as:

$$S_{ij} = \frac{(L_{ij} - \langle L \rangle)}{\langle L \rangle} \quad (1)$$

where L_{ij} is the centroid of the energy spectrum at this position and <L> is the average over the entire crystal. In the case of a crystal with a perfectly uniform response, the variance of S_{ij} would be dictated only by the statistical uncertainty of the centroids of the peaks. In practice, however, the variance of S_{ij} can be dominated by the light output non-uniformity in each crystal.

Two methods are used to correct for non-uniformities in the light output. The first characterizes the non-uniformities using a two-dimensional linear fit to the non-uniformity. The resulting non-linearity parameter F_{ij} is calculated as:

$$F_{ij} = A + Bi + Cj \tag{2}$$

where the parameters A, B, and C are determined from fitting Equation 2 to the non-uniformity across the face of the crystal. Corrected light outputs $S_{ij,corr}$ can then be obtained by dividing individual energy values by $1+F_{ij}$, where F_{ij} are the best-fit values obtained by fitting the data with Eq. 2.

Using Equations 1 and 2, the residual non-uniformity, which could be due to statistical variations in the light output, is defined by subtracting the fitting function from the measured non-uniformity:

$$D_{ij} = S_{ij} - F_{ij} \tag{3}$$

In cases where higher-order corrections are desired due to non-linear non-uniformities or due to lower statistics, smoothed non-uniformities are calculated using a 3x3 flat smoothing function:

$$SM_{ij} = \frac{1}{N_{points}} \sum_{\substack{k=i-1 \\ l=j-1}}^{\substack{k=i+1 \\ l=j+1}} S_{kl} \tag{4}$$

where the summation includes only the values within these limits for k and l at which values of S_{ij} were measured. Consequently, N_{points} =9,6, and 4 for points (i,j) in the center, edge, or corner of the detector, respectively. This increases, by a multiplicative factor of

N_{points}, the effective number of counts in the grid map and thereby reduces the statistical fluctuations.

A similarity between the smoothed non-uniformities for particles with different charge Z, mass A, or energy E was observed. This similarity was probed by determining a scaling factor α(Z,A,E):

$$SM_{ij}(Z, A, E) = \alpha(Z, A, E) \cdot SM_{ij}(Z_0, A_0, E_0) \tag{5}$$

where Z_0=3, A_0=6, and E_0=158 was taken for all comparisons between HiRA detectors tested at the coupled cyclotron facility (CCF) and Z_0=2, A_0=4, and E_0=220 for tests conducted at the Cyclotron Institute at Texas A&M University. The value of α is then determined by fitting the non-uniformity obtained for particles with Z, A and E using Eq. 5 and the reference scan for particles with Z_0, A_0 and E_0.

Residual non-uniformities D'_{ij} in the light outputs can be obtained as discussed previously by subtracting the smoothed non-uniformity SM_{ij} from observed values for S_{ij} similar to the method described in Eq. 3:

$$D'_{ij} = S_{ij} - SM_{ij} \tag{6}$$

If one utilizes the smoothed non-uniformity to make point-by-point corrections to the light output non-uniformity, one can largely correct the observed non-uniformity. After using Eq. 6 to correct according to the smoothed non-uniformity, a simple measure of the residual non-uniformity of the test crystals may be obtained from the rms values for D'_{ij}

$$D'^{2}_{rms} \equiv \frac{N_{points}}{N_{points} - 1} \frac{1}{N_{pixels}} \sum_{ij} \left(S_{ij} - SM_{ij}\right)^2 \tag{7}$$

where SM_{ij} is calculated from Eq. 4, N_{pixels} is the number of pixels included in the sum and N_{points} =9 is the number of parameters used in the smoothing algorithm. These rms values, however, include the statistical fluctuations of the centroids $S_{i,j}$ of the energy spectra, which can be significant if the statistics are limited. From the widths and counts in the peaks, this statistical contribution D_{stat}^2 was calculated and a corrected value $D_{rms,corr}$ was obtained as follows:

$$D_{rms,corr} = \sqrt{D'^2_{rms} - D^2_{stat}} \tag{8}$$

$D_{rms,corr}$ is the contribution to the resolution that is associated with the non-uniformity in the light output. Measurements of the raw, smoothed, and residual non-uniformities are described in the following sections.

Crystal preparation

Light output in thallium doped CsI occurs through the transfer of a small fraction (<10%) of the energy lost in the crystal by the incident ion to the excitation and subsequent radiative decay of thallium dopant ions. The thallium is incorporated into the CsI lattice in molar concentrations of the order of 0.1% during crystal growth [9]. In general, while the light output is caused by the competition between the radiative deexcitations of the thallium dopant ions in the CsI(Tl) crystal and the non-radiative deexcitation of the crystal by other decay modes [10,11], the ionization density of a specific ion dictates the amount of light produced. The competition between radiative and non-radiative deexcitations depends on the thallium doping concentration, the temperature and, possibly, other chemical or physical properties of the crystal.

The observations of local non-uniformities in light output by ref. [5] suggest that changes in the growth procedures for the CsI(Tl) crystals, an accurate compensation of the observed non-uniformities, or a combination of these techniques might lead to an improved energy resolution. The origins of the observed non-uniformities in ref. [5], however, are not understood. They may include local variations in the thallium doping concentrations and possibly, the presence of crystal defects or contaminants [10].

Ten crystals – numbered 0 through 9 – were studied using two beam tests and alpha source scans across the crystal surface. Because the average light output of CsI(Tl) increases strongly with molar doping concentration below about 0.1% and then remains roughly constant above this concentration, the sensitivity to local variations in doping concentration may be minimized by maintaining a high average thallium concentration. To address this possibility, two (30x30x40 mm^3) test crystals (crystals 6 & 7 in Table 1) were prepared with higher nominal thallium concentrations (about 0.5-0.6% molar concentration or 1000 – 1200 ppm Tl as compared to the typical doping concentration of 0.15%-0.35% molar concentration or 300 – 700 ppm Tl). We label these crystals here as "superdoped", even though the doping level of these crystals may not lie far outside of the typical range of doping levels available commercially. Alternatively, an attempt was made to modify the local relative concentrations of thallium dopant ions and defect sites by thermally annealing the crystals in vacuum, a process that has modified the light outputs of some scintillators [12,13]. To address this possibility, six (30x30x30 mm^3) test crystals (crystals 0–5) were prepared. Three of these were annealed (crystals 1, 3 & 5) and three were not annealed (crystals 0, 2 & 4). No specifications or pre-selection criteria regarding the overall non-uniformity were imposed on the test crystals.

Consequently, some of the test crystals displayed larger variations in the light output across the face of the crystal than would be desirable for many applications. We believe this did not negatively impact tests for *local* non-uniformities that depend non-linearly on the position of the ionization trajectory through the crystal. We did not attempt to differentiate between the non-uniformities along the growth axis and the non-uniformities along the other two Cartesian coordinates of each crystal because the orientation of the growth axis with respect to the final crystal surfaces was not recorded and retained.

In addition to the eight test crystals, two final HiRA crystals (crystals 8 and 9) were examined. An acceptance criterion that the light output varies by less than ±0.5% across the face of the detector was placed upon the HiRA crystals. The HiRA crystals, with square 3.5x3.5 cm^2 front and 3.9x3.9 cm^2 rear surfaces and a length of 4 cm, were somewhat larger than the test crystals. Fig. 1 shows side and front views (for a HiRA detector) of the scintillator and photodiode package. Both test and HiRA crystals were prepared by fine polishing the front and rear surfaces, and sanding the four sides with 400 grit paper in the direction from the front surface to the light guide. Light-guides of 1.3 cm thickness were glued to the of the HiRA crystals with BC 600 optical cement and to the six smaller test crystals with GE Bayer Silicones RTV615 silicon rubber glue. The larger (30x30x40 mm^3) test crystals were used without light guides. Silicon photodiodes with a thickness of 0.3 mm and an active area of 18x18 mm^2 were glued to the rear of the light guide with GE Bayer Silicones RTV615 silicon rubber glue. The sides of the test crystals were wrapped using one layer of cellulose nitrate membrane filter paper and then one layer of Teflon tape. The sides of the HiRA crystals were wrapped with two layers of cellulose nitrate filter paper and one layer of aluminized Mylar. The front faces of all

crystals were covered with an aluminized Mylar foil. The light guides were painted with BC-620 reflective paint.

Alpha source measurement configuration

In order to test the position dependence of the response of the CsI crystals to 5.486 MeV alpha particles from a ^{241}Am source, a test apparatus was built, which allows one to move a collimated alpha source and a CsI(Tl) crystal in perpendicular directions inside a vacuum chamber. The configuration was automated such that a spectrum was obtained for points separated by a spacing of 3mm on a 10 by 10 Cartesian grid on the front surface of the test crystals. This grid was centered on the crystals and avoided the edges. At each grid point, the collimated source irradiated a 3 mm diameter area of the crystal surface for 5 minutes before moving to the next grid point. The source test configuration is diagrammed in Fig. 2a.

Beam measurement configurations

While alpha source measurements are practical for pre-scanning large numbers of crystals prior to fabrication into an experimental device, such a test probes only the first 30 microns of the crystal or less. As large doping gradients tend to persist throughout a crystal [1,4,5], such tests can serve to reject crystals with large gradients of order of 1% or more, but may not provide information about the persistence of small non-uniformities of the order 0.1%.

In order to measure the variation of such small non-uniformities throughout the test crystals, the eight test crystals were scanned with primary beams of 220 MeV alpha particles and 110 MeV deuterons from the K500 cyclotron at the Texas A&M cyclotron

facility. The experimental configuration was placed in air at the end of the Single-Event Effect (SEE) beam-line. A 500μm thick double-sided silicon strip detector was fixed in position near the exit foil of the beam pipe in front the crystals. The beam illuminated a circular spot of 2.5 cm diameter on the silicon detector; the 3 mm wide horizontal and vertical strips of this detector divided the beam spot into 100 pixels, each having a size of 3x3 mm^2. The 8 CsI(Tl) crystals were placed behind the silicon detector on a movable computer controlled platform. Thus, the light output uniformity was measured over a Cartesian grid for both the 220 MeV alpha and 110 MeV deuteron beams. Fig. 2b shows a schematic diagram for the two beam test configurations.

A relative comparison of the average light output of the eight test crystals from this beam test is shown in Fig. 3. (Here the data was arbitrarily normalized to that of crystal #6.) Somewhat higher than average light outputs were observed for the "superdoped" crystals 6 &7; however, the range of light outputs is large. On the average, the light output of annealed and non-annealed crystals was comparable. Because light output prior to annealing was not measured, however, this comparison does not probe whether annealing enhances the light output of a specific crystal.

Beam scans of four HiRA crystals were also performed using secondary projectile fragmentation beams from the CCF at Michigan State University. Secondary beams of 53 MeV protons, 48 MeV ^{3}He, 40 MeV deuterons, 105 MeV ^{3}He, 158 MeV ^{6}Li, and 243 MeV ^{7}Be were produced by fragmenting a primary ^{40}Ar beam at E/A=140 MeV on a Be target and selected by magnetic rigidity with the A1900 separator. For each beam, a 1% separator momentum acceptance was used corresponding to an energy resolution of 2%. The configuration for the experiment was placed in air in the N3 vault. A 1500μm thick

double-sided HiRA silicon strip detector with an active area of about 64x64 mm^2 was fixed in position in front of the four CsI(Tl) detectors to form a energy loss telescope. This telescope was mounted on a movable platform in front of the exit foil of the beam pipe. Computer controlled stepping motors were used to move each crystal to illuminate uniformly most of its surface area with the beam. In this fashion, the light output for each HiRA crystal was measured over a 256 pixel Cartesian grid with a pixel size of 2x2 mm^2 for all fragmentation beams.

Alpha source scanning results

The centroid of the light output peak was calculated for each of the Cartesian grid points. Fig. 4a shows S_{ij} calculated from Equation 1 for a crystal (#4) with a large non-uniformity. (In order to minimize sensitivity to edge effects, we have excluded the outside points (pixels 1 and 10) from this figure and for all subsequent plots of the alpha source and the various beam scans.) Fig. 4b shows S_{ij} for a crystal (#6) with a small non-uniformity. The overall non-uniformities in light output for the final HiRA crystals were specified to be less than ±0.5%; plots of the overall light output uniformities of HiRA crystals were therefore more similar to Fig. 4b than to Fig. 4a.

Fit parameters B and *C,* which describe the linear variation in the light output (in %) for the test crystals, are given in Table 2. For reference, a value of 0.1 (0.05) for B or C implies an increase of 1% (0.5%) in the light output across the 3 cm wide crystal

Beam scanning results

Fewer beams were used for scanning the test crystals than for the final HiRA crystals, but the resolution of the primary beams used for the test crystals was superior to that of the

secondary beams used for the final HiRA crystals. The results of these two beam scans are therefore discussed separately.

Results for the test crystals

As stated above, the beam test consisted of a 220 MeV alpha beam and a 110 MeV deuteron beam. The penetration depth for the alpha beam is about 11 mm, and the penetration depth for the deuteron beam is about 22 mm, which are both much larger than the penetration depth ~ 30 μm for the ^{241}Am source [14]. The 3x3 mm^2 spots defined by the silicon detector defined the trajectories of the alphas and deuterons through the crystals. The transverse straggling of 0.5 mm for the alpha beam and 1.3 mm for the deuteron beam did not exceed the pixel spatial resolution. Values for S_{ij} were calculated at each grid point for each detector for both alpha and deuteron runs.

Figs. 5a and 5b show S_{ij} obtained with the alpha beam for the same crystals with large and small non-uniformities shown in Figs. 4a and 4b, respectively. The corresponding plots for the deuteron beam are shown in Figs. 5c and 5d, respectively. Again for the beam scans, one observes a roughly linear dependence of S_{ij} on the displacement across the face of crystal #4, while no strong linear dependence is observed for crystal #6. The light output L_{ij} was fit assuming a linear dependence of the form given by Eq. 2. Values for B and C for the test crystals are given in Table 2. Fig. 6 shows the correlation between the parameters B and C obtained from the alpha source fits and those obtained from the 220 MeV alpha beam (solid points) or the 110 MeV deuteron beam (open points). The slope of the dashed trendline shown in the figure has a value of 0.5. Thus the alpha source scan is twice as sensitive to the crystal non-uniformity than are the alpha and deuteron beam scans; the alpha source sensitivity is actually more comparable to that for

beam particles of much higher Z such as lithium, see below. Some of the difference between the linear fit parameters of the alpha scan and the beam scans may be due to non-zero doping gradients in the beam direction; the ^{241}Am alpha-scan particles, the 220 MeV alpha beam particles, and the 110 MeV ^{2}H beam particles have very different penetration depths. However, we will show that the light output non-uniformity is larger for particles with larger average stopping powers in the crystal; these average stopping powers are greater for the alpha source than for the alpha beam and both alpha source and beam have larger average stopping powers than those of the deuteron beam. This is probably the main reason why the non-uniformities observed for the alpha source exceed those for the alpha and deuteron beams.

The correlation between the various scans shows why one can use the alpha source measurements to preselect the crystals and reject crystals with large non-uniformities. The vertical lines indicate the acceptance criterion $|\text{alpha source parameter}| < 0.1$; crystals to the left of the leftmost line and to the right of the rightmost line, which displayed large non-uniformities in both the beam and alpha source tests, are rejected under this criterion.

Residual non-uniformities calculated with Equation 3 are shown in Fig. 7 for the same crystals #'s 4 and 6. The residual non-uniformities are zero on the average, but there are regions in which all the neighboring pixels have positive residuals and other regions where all the neighboring pixels have negative residuals. This suggests that a much higher order fit or a pixel-by-pixel correction to the light output uniformity might be a better approach. This is particularly true for crystal #6, which displays some ridges of higher light output in both panels (b) and (d).

By combining the energy deposited in the silicon with the energy deposited in the CsI(Tl) crystal one obtains measurements of the total beam energy of the incident deuteron and alpha beams. These are shown in Fig. 8 for alpha particles (bottom panels) and deuterons (top panels). The left panels are for the less uniform CsI(Tl) crystal (#4) and the right panels are for the more uniform CsI(Tl) crystal (#6). The dotted lines are the overall crystal energy spectra without correction for the light output non-uniformity. The dashed lines are the crystal spectra corrected with the linear fit for the light output non-uniformities. The solid lines are spectra for particles that enter into one randomly chosen pixel in the detectors. This latter spectrum has the same resolution (e.g. crystal #6: $\sigma \approx$ 0.15% or 0.16 MeV for deuterons, 0.15% or 0.33 MeV for alphas) that one would achieve by a pixel-by-pixel correction for the light output non-uniformity across the crystal. The difference between the solid histograms and dashed lines reflects the degree to which the non-uniformities can be modeled by a linear dependence. Crystal #4 is more linear in its non-uniformity than crystal #6; the corrected non-uniformity of crystal #4 shown in Fig. 7 is smaller than the corresponding corrected non-uniformity of crystal #6. Thus, the corrected resolution for crystal #4, shown by the dashed line in the left panel of Fig. 8, is smaller than that of crystal #6, shown in the right panel. It is concluded that the non-uniformity varies linearly across the face of crystal 4, while the variation is more complex across crystal 6.

The energy resolution of the beam makes a negligible contribution to the resolution of a single pixel given by the solid histograms. The electronic noise (determine by a precision pulser) contributes $\sigma_{noise} \approx 0.1$ MeV to the single pixel resolution. This corresponds to rms contributions of 0.1% for deuterons and 0.05% for alphas. Subtracting this electronics

noise contribution, one obtains rms intrinsic (noise corrected) resolutions of about 0.11% (≈0.1 MeV) for deuterons and 0.14% (≈0.3 MeV) for alphas.

Results for the HiRA crystals

Figs. 9 and 10 show S_{ij} obtained for two HiRA crystals (8 & 9) for proton, deuteron, ^{3}He (105 MeV), ^{6}Li and ^{7}Be fragmentation beams. Unlike the case for the test crystals with larger thallium doping gradients, S_{ij} does not display a strong linear dependence across the face of each detector. In fact, the observed non-uniformities are rather complex and would require rather high order polynomials or Fourier components to achieve a satisfactory fit. On the other hand, the trends for the different particle types are similar in form. The magnitudes of the non-uniformities are larger for more highly charged particles such as ^{7}Be or ^{6}Li than for protons or deuterons.

It is interesting that the similarity in form for the non-uniformity persists when the ranges of the various particles, given in Table 3, differ somewhat. (Here, one should focus on the upper six rows, which correspond to the data in Figs. 9 and 10.) This suggests that an accurate measurement of the non-uniformity with one particle species may allow one to predict the light output for other species for a variety of ranges in the neighborhood of the range of the measured species. If measurements could be performed with very high statistics by increasing the test time by about an order of magnitude and if one where not worried about radiation damage to the silicon detectors, the response could be measured for every particle species on a pixel-by-pixel basis. In practice, however, such a practice is expensive and therefore unlikely. To allow non-uniformity studies with more limited statistical accuracy, the smoothing algorithm given by Equation 4 was developed. In the

calculation of the scaling parameter α (Equation 5), comparisons of all particles were made to 158 MeV ^{6}Li

Figs. 11 and 12 show the smoothed distributions for the various particles for these two crystals. Fig. 13 shows the same smoothed distributions for 39 MeV deuterons, scaled by the parameter α (in black) along with the ^{6}Li (in red) non-uniformities. This rescaling procedure works remarkably well; the smoothed ^{6}Li non-uniformities are rather similar to the smoothed, scaled non-uniformities for the other particle types. The values for the scaling parameters are given in Table 3. In general, the scaling parameters increase with charge, reflecting the fact that the non-uniformities observed for highly charged particles are larger.

This method has also been applied to the test crystals (#'s 0-5); here the ^{4}He data were used as the reference for scaling purposes. Comparisons of the smoothed and rescaled non-uniformities for deuterons and alphas in crystals #4 and #6 are shown in Fig. 14. Assuming that the non-uniformity varies continuously with the depth, we expect differences in the non-uniformities observed at different depths. The deuterons sample the crystal non-uniformities over a much greater depth (2.2 cm) compared to the alpha particles (1.1 cm). Even though, the differences shown in the figure are small, we think one should be cautious about assuming that scaling can be accurately applied when particle have very different ranges. The scaling factors for deuterons (with respect to α particles), shown in Table 3, are different for the two crystals, suggesting problems with the scaling concept when the two particles have significantly different ranges; however, the value of α for crystal 6 also has a large uncertainty due to the fact that the smoothed non-uniformities for this crystal are small.

Energy spectra, corrected according to the smooth non-uniformities, are compared to the uncorrected crystal and single-pixel energy spectra in Fig. 8 (dot-dash line). It can be seen that the method of correcting by smoothing is a useful algorithm for correcting non-uniformities, reducing the resolution in the deuteron spectra to nearly that of a single pixel. In the alpha spectra, where the noise contribution is less, the accuracy of this approach is more sensitively tested. In particular, the prominent ridges in the alpha spectra for crystal #6 that can be seen in Fig. 7b cannot be completely corrected by the smoothing algorithm. If it were necessary, in principle, higher statistics scans could be performed and such rapidly changing non-uniformities could be corrected by a pixel-by-pixel map that could then be propagated to the other particles that have approximately the same ranges in the crystal.

Some insights into the charge dependence of the non-uniformities can be obtained if one considers an approximate formulae for the light output given by Birks [10,11]

$$\frac{dL}{dx} = a\left|\frac{dE}{dx}\right| \frac{1}{1 + b\left|dE/dx\right|} \tag{9}$$

where a is a charge independent constant describing the conversion of energy loss into light and b is a charge independent constant describing how the light is quenched in regions of higher energy loss due to a saturation of the CsI(Tl) activation centers near the region of high ionization density. This latter factor is responsible for the observed fact that $\frac{dL}{dx}$ decreases with charge [4,5,9-11]. It explains the stronger non-linearities in the energy calibrations for heavily ionizing particles and, in the context of this simple model,

is the likely origin of the charge dependence of the non-uniformities shown in Figs. 9 and 10.

Approximating the stopping power by $\left|\frac{dE}{dx}\right| \approx c\frac{Z^2}{v^2}$, where c is a constant and v is the velocity of the particle and integrating Eq. 9 over the ion's range in the CsI(Tl) detector, yields

$$L \approx aE\left(1+\frac{bcAZ^2}{E}\ln\left(\frac{bcAZ^2/E}{1+bcAZ^2/E}\right)\right) \tag{10}$$

Both the constants a and b in Eqs. 9 and 10 may depend on the position where the ion traverses the crystal; of these two, only the position dependence of b can give rise to the non-uniformities displayed in Figs. 9 and 10. According to Eq. 10, the sensitivity to b is proportional to the stopping power; this suggests that the scaling factors $\alpha(Z,A,E)$ may also be proportional to the stopping power. A plot of $\alpha(Z,A,E)$ as a function of AZ^2/E is examined in Fig. 15. Errors bars are derived by considering the increase in α necessary to change the χ^2 value for the fit by one. A monotonic dependence of $\alpha(Z,A,E)$ on AZ^2/E is observed in support of this ansatz. There may exist a more accurate scaling relationship than this one depending on AZ^2/E, but a more complete set of data would be required to demonstrate it.

Residual non-uniformities D'_{ij} are shown in Figs. 16 and 17 for crystals 8 and 9 and the same incident particles as shown in Fig. 9 and 10. The residual light output variations are zero on the average and for the most part fluctuate about zero randomly, in contrast to the case for test crystals where there were regions in which all neighboring pixels have

positive residuals and other regions where the neighboring pixels have negative residuals. In principle, the removal of such correlated non-uniformities should lead to an improvement in the overall resolution.

Residual non-uniformities after correction for the global non-uniformity

Values of the statistical contribution D_{stat} to the residual non-uniformity in Equation 8 are typically about 0.002% for both the α-beam test and the ^{2}H-beam test. For the HiRA test crystal runs, which have somewhat lower statistics, as well as a larger momentum acceptance, the values of D_{stat} are about 0.01% for all particles used.

The dependence of $D_{rms,corr}$ on the crystal number for the test crystal measurements is given in Table 1 for the two beams. No obvious trends with crystal manufacturing process are observed for the test crystals. The dependence of $D_{rms,corr}$ on particle type is given in Table 4. The values for $D_{rms,corr}$ increase somewhat with the charge of the incident particle. This shows that there are residual non-uniformities that are not well removed by the smoothing procedure, even when neighboring pixels are only 2 mm apart. Of course, these non-uniformities could be more accurately removed for particles with similar penetration depths into the crystal by making a pixel-by-pixel correction or by smoothing over a smaller number of pixels. Whether or not this can be done for individual crystals to the required degree of accuracy depends on the beam time that can be allocated to calibration purposes.

Discussion and Conclusion

We have investigated the non-uniformities observed in ref. [5] for crystals manufactured by several different methods. These measurements reveal the dependencies of the non-

uniformities upon the energy loss of the stopped particle. The subsequent analyses also tested different methods for correcting the measured light outputs for this non-uniformity.

It is natural that accurate pixel-by pixel correction would provide superior results. When faced with the necessity of measuring non-uniformities at a range of depths and for many different particle species, however, it is advantageous to smooth the non-uniformity plots or fit them to a linear function in order to extract the same information from data of lower statistical accuracy than would be required for an accurate pixel-by-pixel correction. We find that a smoothed pixel-by-pixel correction is useful in nearly any case, while the linear correction is useful only in a few special cases, such as those with a large light output gradient across the crystal face. In cases in which the light output or its gradient is not as uniform, the pixel-by-pixel correction utilizing the smoothing algorithm is superior.

None of the different manufacturing methods was obviously superior in suppressing the local variations of the light output that occur over distance scales of the order of a few mm. These local variations are always present; the magnitude of these light output variations, however, depends on the ion. As would be predicted by the non-linearities in the light-output energy loss relationship described by Eqs. 9 and 10, the observed non-uniformities increase with stopping power. This suggests that the non-uniformities reflect saturation and quenching effects that prevail in the sections of the particle's trajectory where the ionization density is largest.

The scaling behavior that is illustrated by Figs. 11 and 12 suggests that a practical correction to these local non-uniformities may be obtained by measuring them for a highly ionizing particle and scaling them down to obtain the corresponding corrections

for more weakly ionizing particles. Clearly, this correction is more accurate when the light output non-uniformity for highly ionizing particles is smaller. While the present analyses suggests this is a promising approach that can achieve final non-uniformities in the order of 0.1%, it is still not clear how far one can extrapolate such measured non-uniformities to particles with different penetration depths within the crystals. In principle, the light output also reflects variations in the thallium doping along the ionization trajectory and may lead to different non-uniformities for particles of different range. Thus, measurements of the non-uniformity at different penetration depths are advisable to achieve an accurate overall non-uniformity correction.

This work is supported by the National Science Foundation under Grant Nos. PHY-01-10253, PHY-00-70818, and PHY- 00-70161

References:

1. W.G. Gong, Y.D. Kim, G. Poggi, Z. Chen, C.K. Gelbke, W.G. Lynch, M.R. Maier, T. Murakami, M.B. Tsang, H.M. Xu and K. Kwiatkowski, Nucl. Instr. and Meth. A, **268** (1988) 190.
2. D.W. Stracener, D.G. Sarantites, L.G. Sobotka, J. Elson, J.T. Hood, Z. Majka, V. Abenante, A. Chbihi, D.C. Hensley, Nucl. Inst. and Meth. A, **294** 485 (1990).
3. D. Sarantites, P.F. Hua, M. Devlin, L.G. Sobotka, J. Elson, J.T. Hood, D.R. LaFosse, J.E. Sarantites, M.R. Maier, Nucl. Inst. and Meth. A, **381** 418 (1996).
4. R.T. DeSouza, N. Carlin, Y.D. Kim, J. Ottarson, L. Phair, D.R. Bowman, C.K. Gelbke, W.G. Gong, W.G. Lynch, R.A. Pelak, T. Peterson, G. Poggi, M.B. Tsang, and H.M. Xu, Nucl. Inst. and Meth. A, 295, 109 (1990).
5. A. Wagner, W.P. Tan, B. Davin, K. Chalut, R.J. Charity, Y. Larochelle, M.D. Lennek, T.X. Liu, X.D. Liu, W.G. Lynch, A.M. Ramos, R. Shomin, L.G. Sobotka, R.T. de Souza, M.B. Tsang, G. Verde, H.S. Xu, Nucl. Instr. Meth. A 456, 290 (2001).
6. I. Iori, et al., Nucl. Inst. Meth. Phys. Res. A325, 458 (1993).
7. A. R. Gabler, W. Döring, M. Fuchs, B. Krusche, V. Metag, R. Novotny, M. Röbig-Landau, H. Ströher, V. Tries, C. Molenaar, H. Löhner, J. H. G. van Pol, A. Raschke, M. Sumbera, L. B. Venema, H. W. Wilschut, R. Averbeck, W. Niebur, A. Schubert, R. S. Simon, R. Beck, J. Peise, G. J. Miller, R. O. Owens and G. Anton, Nucl. Instr. and Meth. **346**, (1994) 168.
8. F. Cavallari, Nucl. Instr. and Meth. A, **461** (2001) 368.
9. P. Schotanus, and R. Kamermans, IEEE Trans. Nucl. Sci. 37, (1990) 177.
10. J.B. Birks, Theory and Practice of Scintillation Counters, Pergammon Press (1964).
11. M. Parlog, B. Borderie, M.F. Rivet, B. Tabacaru, A. Chbihi, M. Elouardi, N. Le Neindre, O. Lopez, E. Plagnol, L. Tassan-Got, G. Auger, C.O. Bacri, N. Bellaize, F. Bocage, R. Bougault, B. Bouriquet, R. Brou, P. Buchet, J.L. Charvet, J. Colin, D. Cussol, R. Dayras, A. Demeyer, D. Dore, D. Durand, J.D. Frankland, E. Galichet, F. Genouin-Duhamel, E. Gerlic, S. Hudan, D. Guinet, P. Lautesse, F. Lavaud, J.L. Laville, J.F. Lecolley, C. Leduc, R. Legrain, M. Louvel, A.M. Maskay, L. Nalpas, J. Normand, J. Peter, E. Rosato, F. Saint-Laurent, J.C. Steckmeyer, B. Tamain, O. Tirel, E. Vient, C. Volant, J.P. Wieleczko, Nucl. Inst. Meth. A 482, (2002) 674.
12. S. Burachas et al., NIM. A 486 (2002) 83.
13. F. A. Danevich, A. Sh. Georgadze, V. V. Kobychev, B. N. Kropivyansky, A. S. Nikolaiko, O. A. Ponkratenko, V. I. Tretyak, S. Yu. Zdesenko, Yu. G. Zdesenko, P. G. Bizzeti, T. F. Fazzini, and P. R. Maurenzig, Phys. Rev. C **62**, 045501 (2000).
14. The ranges and transverse straggling values were calculated using the program SRIM 2003 of J.F. Ziegler.

Table 1: $D_{rms,corr}$ (in %) for different particles in the test crystal beam test

Crystal	Crystal type	$D_{rms,corr}$ (%)	
		α Beam	^{2}H Beam
1	Annealed	0.10	0.06
2	Normal	0.09	0.05
3	Annealed	0.07	0.05
4	Normal	0.04	0.03
5	Anneal	0.08	0.07
6	Super-doped	0.11	0.06
7	Super-doped	0.05	0.03

Table 2: Linear fit parameters for Eq.2 for the test crystals determined from α source scanning, α beam measurements and deuteron beam measurements. Crystal types are N=normal, A=annealed, and S=Super-doped. Parameters are in percent.

Crystal	Type	Source	A (%)	B (%)	C (%)
0	N	α Scan	1.496	-0.128	-0.146
		α Beam	-	-	-
		^{2}H Beam	-	-	-
1	A	α Scan	0.832	-0.049	0.061
		α Beam	-0.028	-0.024	-0.010
		^{2}H Beam	0.158	-0.048	0.029
2	N	α Scan	-0.736	-0.090	0.275
		α Beam	0.017	-0.055	0.058
		^{2}H Beam	0.471	-0.088	0.048
3	A	α Scan	0.580	-0.258	0.012
		α Beam	0.220	-0.132	0.067
		^{2}H Beam	0.153	-0.110	0.071
4	N	α Scan	-0.516	-0.086	0.218
		α Beam	-0.028	-0.051	0.043
		^{2}H Beam	-0.097	-0.048	0.082
5	A	α Scan	1.342	-0.099	-0.149
		α Beam	1.194	-0.113	-0.107
		^{2}H Beam	0.892	-0.063	-0.061
6	S	α Scan	-0.136	-0.023	0.015
		α Beam	-0.124	0.013	-0.003
		^{2}H Beam	-0.145	-0.001	0.034
7	S	α Scan	-0.229	0.000	0.040
		α Beam	-0.011	0.018	-0.037
		^{2}H Beam	0.333	-0.027	0.019

Table 3: Values for the scaling parameter $\alpha(Z,A,E)/\alpha(3,6,158)$. The last two rows correspond to the scaling with respect to 220 MeV α particles in the indicated crystals.

Particle	Energy (MeV)	Range (mm)	α
p	53	10.3	0.509
^{2}H	39	3.8	0.608
^{3}He	48	1.0	0.965
^{3}He	105	3.8	0.927
^{6}Li	158	2.1	1.000
^{7}Be	243	2.2	1.048
^{2}H (CsI #4)	110	22.2	0.997
^{2}H (CsI #6)	110	22.2	0.230

Table 4: $D_{rms,corr}$ for different particles in the HiRA beam test.

Particle	Incident Energy	Range in CsI (mm)	$D_{rms,corr}$ (%)	
			CsI 8	CsI 9
p	53	10.3	0.08	0.07
^{2}H	39	3.8	0.08	0.06
^{3}He	48	1.0	0.11	0.09
^{3}He	105	3.8	0.11	0.11
^{6}Li	158	2.1	0.13	0.13
^{7}Be	243	2.2	0.26	0.16

Figure Captions:

Fig. 1: Side view and front view of a HiRA crystal, light guide and photo-tube assembly. Two inner sides of the crystal are cut perpendicular to the front and rear faces of the crystal and two outer sides of the crystal are cut at an angle of 5.3° from the perpendicular in order to back the active area of the silicon detectors when the telescopes are placed at a distance of 35 cm.

Fig. 2: Test configurations for the HiRA CsI crystals. Figure a shows the configuration for the alpha source scanning test. Figure b shows the beam test configuration. In the case of the test at the Texas A&M facility, the silicon detector was stationary with respect to the beam line. In the case of the tests performed at the NSCL, the silicon detector moved with the crystals.

Fig. 3: Relative comparisons of the light outputs for the eight test crystals. The light outputs of the HiRA crystals were selected to be within 15% of the light output of test crystal 6. These results were obtained with the 220 MeV α beam; the same results are obtained for the deuteron beam. The error bars are estimated from the reproducibility in the relative light output observed after recoupling these test crystals to the photo-diode and its associated electronics.

Fig. 4: The variation of the light output over the face of the detector is shown here as a percent deviation from the mean (S_{ij} as defined in Eq. 1). Here neighboring pixels are separated from each other by 3 mm in both x and y directions. This result is obtained for crystals #4 and #6 (Figures a and b, respectively) using 5.5 MeV alphas from a ^{241}Am source. The standard deviation of S_{ij}, i.e. $\sqrt{\langle S_{ij}^2 \rangle}$ is also given.

Fig. 5: Panels 5a and 5b show S_{ij} obtained for the alpha beam with crystals #4 and #4 - the same crystals with a large and small non-uniformities shown in Figs. 3a and 3b, respectively. The corresponding plots for the deuteron beam are shown in Panels 5c and 5d respectively. The standard deviation of S_{ij}, i.e. $\sqrt{\langle S_{ij}^2 \rangle}$ is also given.

Fig. 6: Correlation between the slope parameters obtained via the alpha source test and those obtained via the 220 MeV alpha beam test (solid points) and the 110 MeV deuteron beam test (open points).

Fig. 7: Panels 7a and 7b shows D_{ij} obtained for the alpha beam using crystals #4 and #6 as in Figure 3 and 5. The corresponding plots for the deuteron beam are shown in Panels 7c and 7d, respectively. The standard deviation of D_{ij}, i.e. $\sqrt{\langle D_{ij}^2 \rangle}$ is also given.

Fig. 8: Left panels: CsI(Tl) crystal #4 with large non-uniformity. Right panels: CsI(Tl) crystal #6 with small non-uniformity. Bottom panels: Results for 110 MeV deuterons. Top panels: Results for 220 MeV alpha particles. In all panels, the dotted lines are the uncorrected energy spectra. The dashed lines are the spectra corrected with the linear correction for the light output non-uniformities. The solid lines are spectra for particles that enter into one randomly chosen pixel in the detectors. The dot-dash line is the crystal spectra corrected using the smoothing algorithm described in the text.

Fig. 9: Non-uniformity values S_{ij} (in) for HiRA crystals #8 (left side) and #9 (right side) for the indicated beam particles from the CCF of the NSCL. Each pixel is separated in

both x and y directions from its neighbor by 2 mm. The standard deviation of S_{ij}, i.e. $\sqrt{\langle S_{ij}^2 \rangle}$ is also given.

Fig. 10: Non-uniformity values S_{ij} (in) for HiRA crystals #8 (left side) and #9 (right side) for ^{6}Li and ^{7}Be fragmentation beams from the CCF of the NSCL. The standard deviation of S_{ij}, i.e. $\sqrt{\langle S_{ij}^2 \rangle}$ is also given.

Fig. 11: Smoothed non-uniformity values SM_{ij} in crystals #8 (left side) and #9 (right side) for protons, deuterons, and ^{3}He's measured in the HiRA beam test. The rms values of the smoothed distributions are also shown.

Fig. 12: Smoothed non-uniformity values SM_{ij} for crystals #8 (left side) and #9 (right side) for ^{6}Li and ^{7}Be beams measured in the HiRA beam test. The rms values of the smoothed distributions are also shown.

Fig. 13: The smoothed distributions for deuterons (in black) along with scaled ^{6}Li non-uniformities (in red) for crystals #8 (left) and #9 (right). The rms values of the smoothed distributions are also shown.

Fig. 14: The smoothed distributions for deuterons (in black) along with scaled ^{4}He non-uniformities (in red) for crystals #4 (left) and #6 (right). The rms values of the smoothed distributions are also shown.

Fig. 15: Scaling factor α, which describes the non-uniformity of specific isotopes with respect to that for ^{6}Li at E/A=26 MeV for various particles and energies. By construction, we have a value of α=1 at AZ^2/E=0.34 corresponding to the ^{6}Li fragmentation beam. The line is the fit to the non-linear term in Eq. 10.

Fig. 16: Residual non-uniformity $D'_{ij}=S_{ij}-SM_{ij}$ for protons (top), deuterons (middle), and ^{3}He (bottom) particles on crystals #8 (left) and #9 (right). The rms values of the corrected distributions are also shown. The large residual non-uniformities around X-Pixel=14 and Y-Pixel=2 are due to low statistics of the scan.

Fig. 17: Residual non-uniformity $D'_{ij}=S_{ij}-SM_{ij}$ for ^{6}Li (top) and ^{7}Be (bottom) using crystals #8 (left) and #9 (right). The rms values of the corrected distributions are also shown.

Fig. 1 Side view and front view of a HiRA crystal, light guide and photo-tube assembly. Two inner sides of the crystal are cut perpendicular to the front and rear faces of the crystal and two outer sides of the crystal are cut at an angle of 5.3° from the perpendicular in order to back the active area of the silicon detectors when the telescopes are placed at a distance of 35 cm.

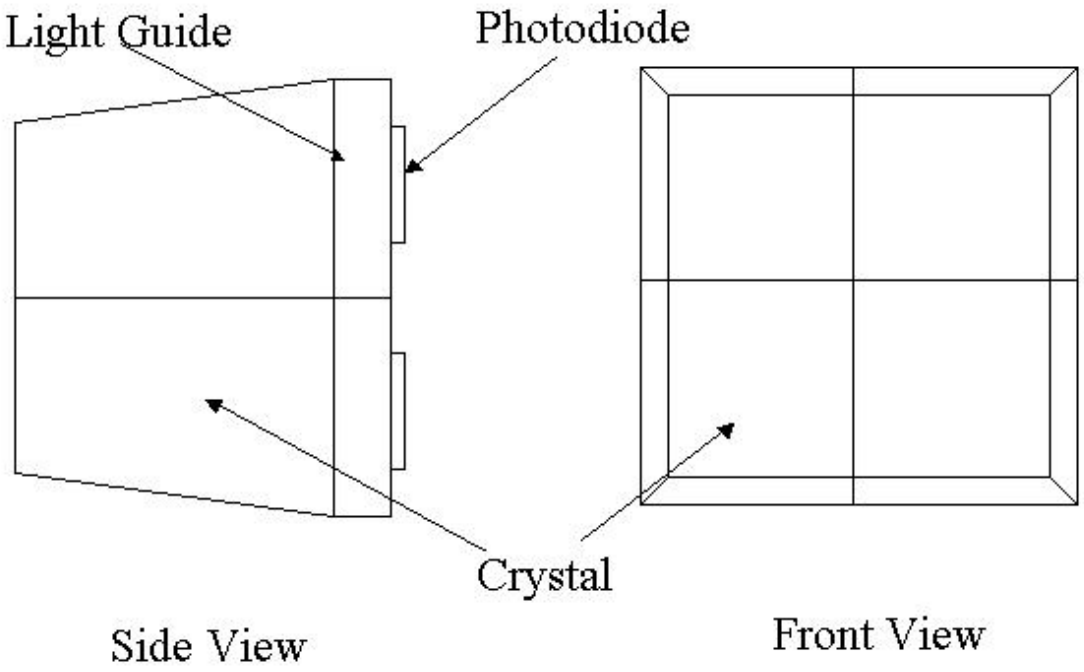

Fig. 2: Test configurations for the HiRA CsI crystals. Figure a shows the configuration for the alpha source scanning test. Figure b shows the beam test configuration. In the case of the test at the Texas A&M facility, the silicon detector was stationary with respect to the beam line. In the case of the tests performed at the NSCL, the silicon detector moved with the crystals.

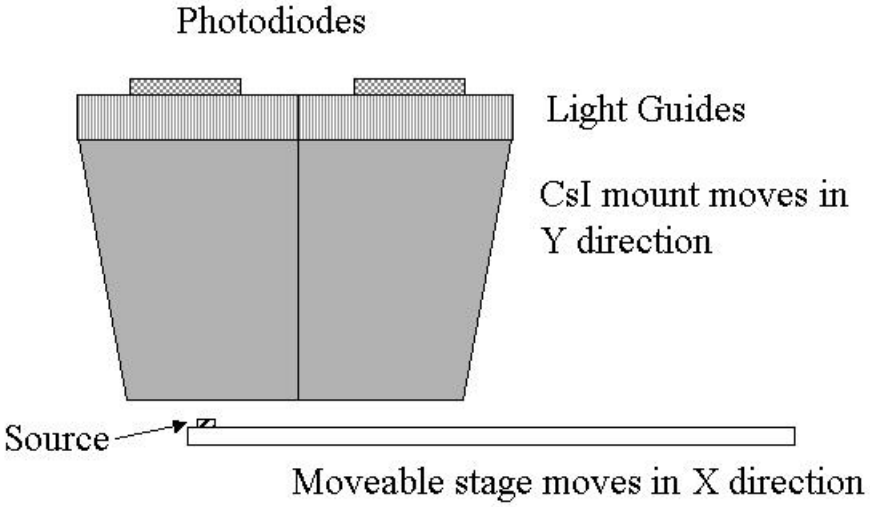

(a)

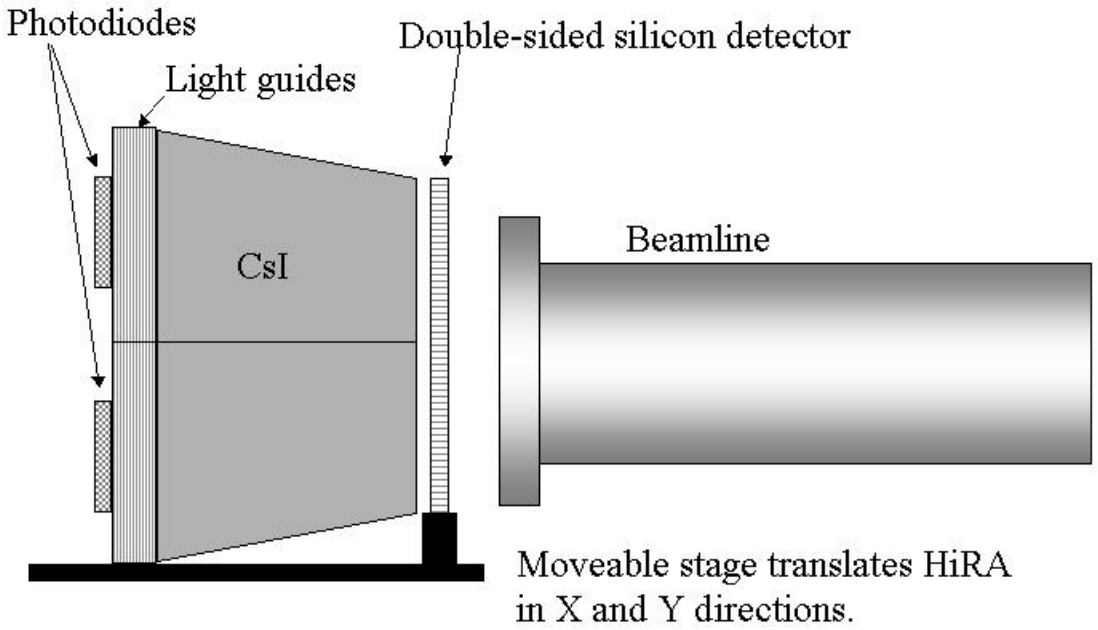

(b)

Fig. 3: Relative comparisons of the light outputs for the eight test crystals. The light outputs of the HiRA crystals were selected to be within 15% of the light output of test crystal 6. These results were obtained with the 220 MeV α beam; the same results are obtained for the deuteron beam. The error bars are estimated from the reproducibility in the relative light output observed after recoupling the test crystals to the photo-diode and its associated electronics.

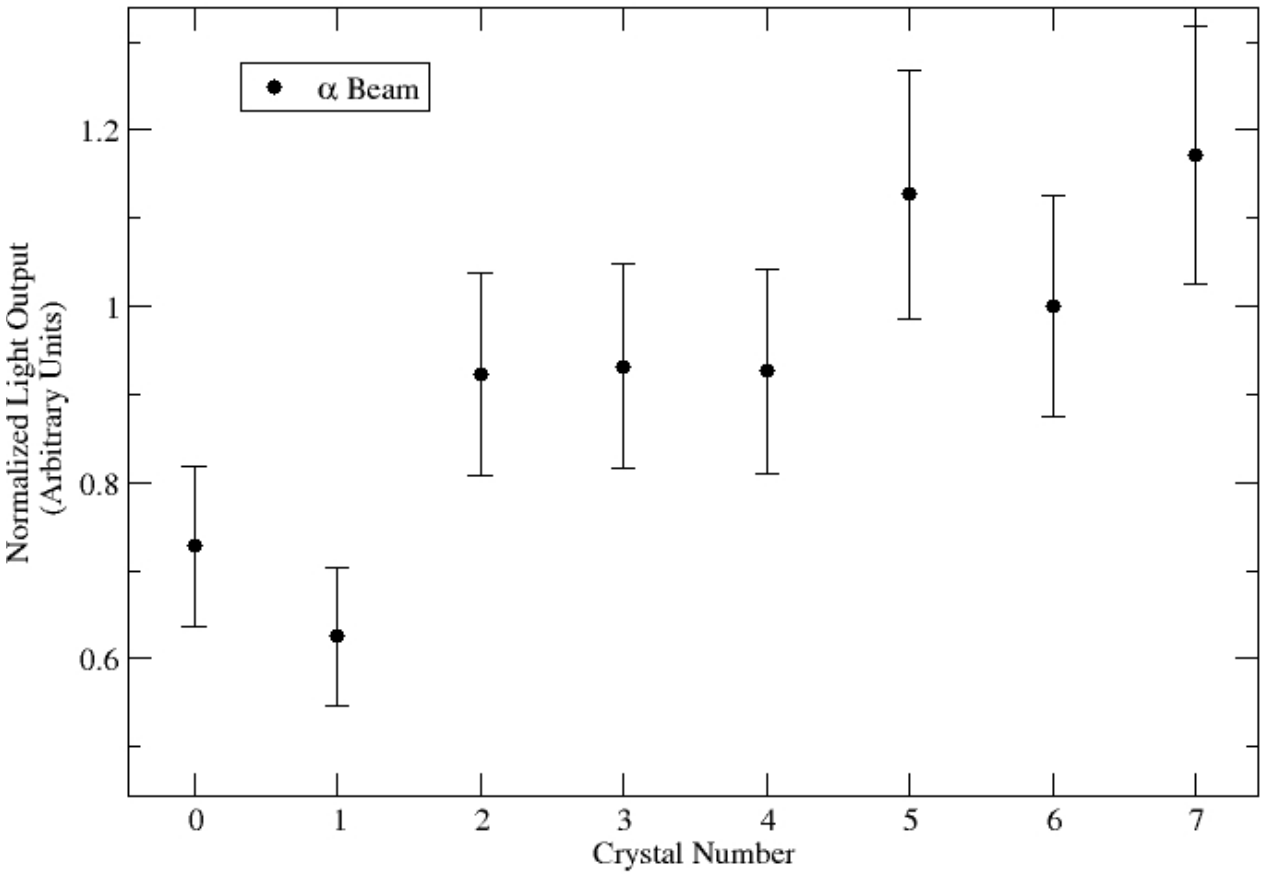

Fig. 4: The variation of the light output over the face of the detector is shown here as a percent deviation from the mean (S_{ij} as defined in Eq. 1). Here neighboring pixels are separated from each other by 3 mm in both x and y directions. This result is obtained for crystals #4 and #6 (Figures a and b, respectively) using 5.5 MeV alphas from a ^{241}Am source. The standard deviation of S_{ij}, i.e. $\sqrt{\langle S_{ij}^2 \rangle}$ is also given.

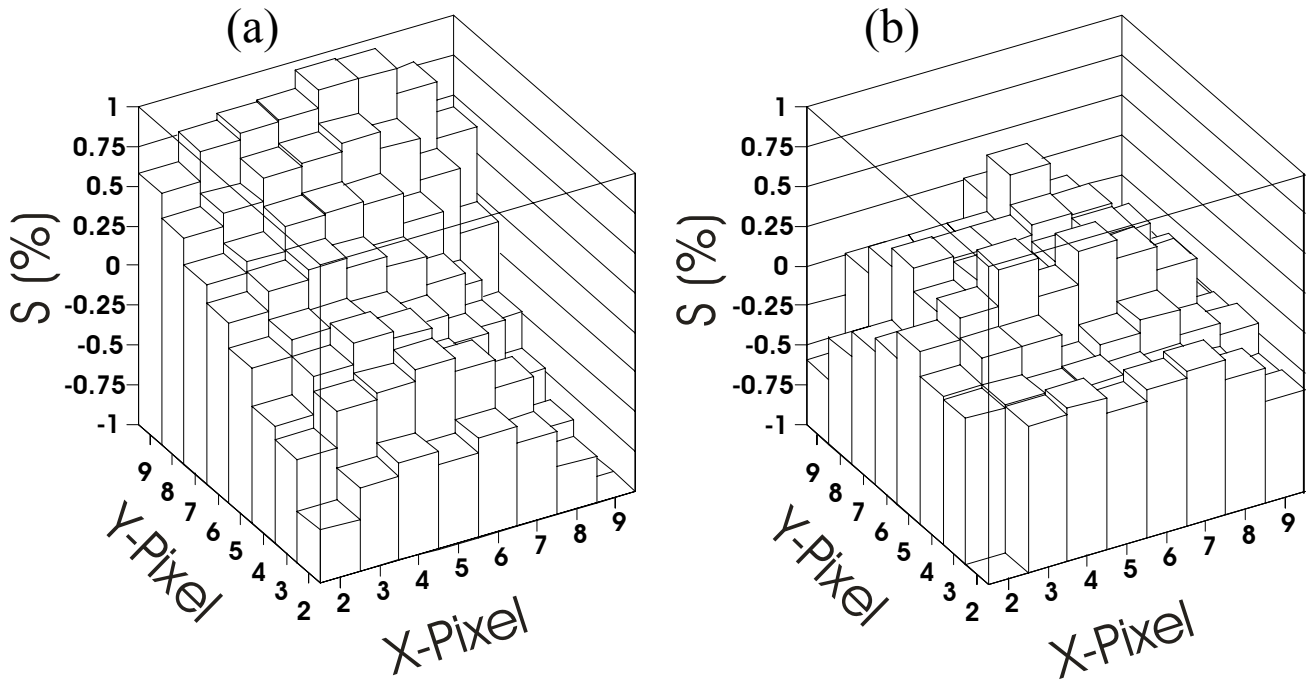

S_{rms}=0.539%

S_{rms}=0.271%

Fig. 5: Panels 5a and 5b show S_{ij} obtained for the alpha beam with crystals #4 and #4 - the same crystals with a large and small non-uniformities shown in Figs. 3a and 3b, respectively. The corresponding plots for the deuteron beam are shown in Panels 5c and 5d respectively. The standard deviation of S_{ij}, i.e. $\sqrt{\langle S_{ij}^2 \rangle}$ is also given.

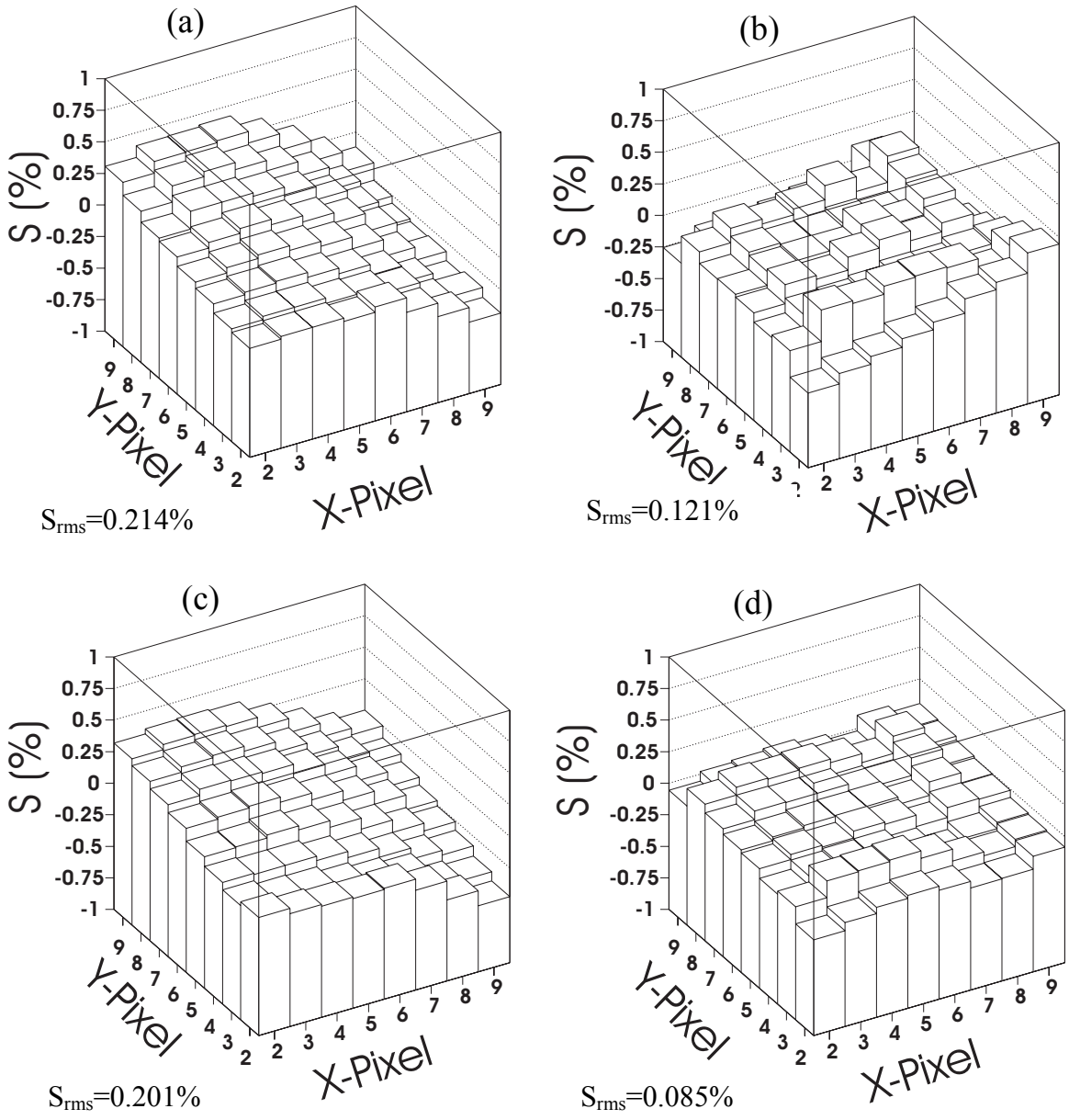

Fig. 6: Correlation between the slope parameters obtained via the alpha source test and those obtained via the 220 MeV alpha beam test (solid points) and the 110 MeV deuteron beam test (open points).

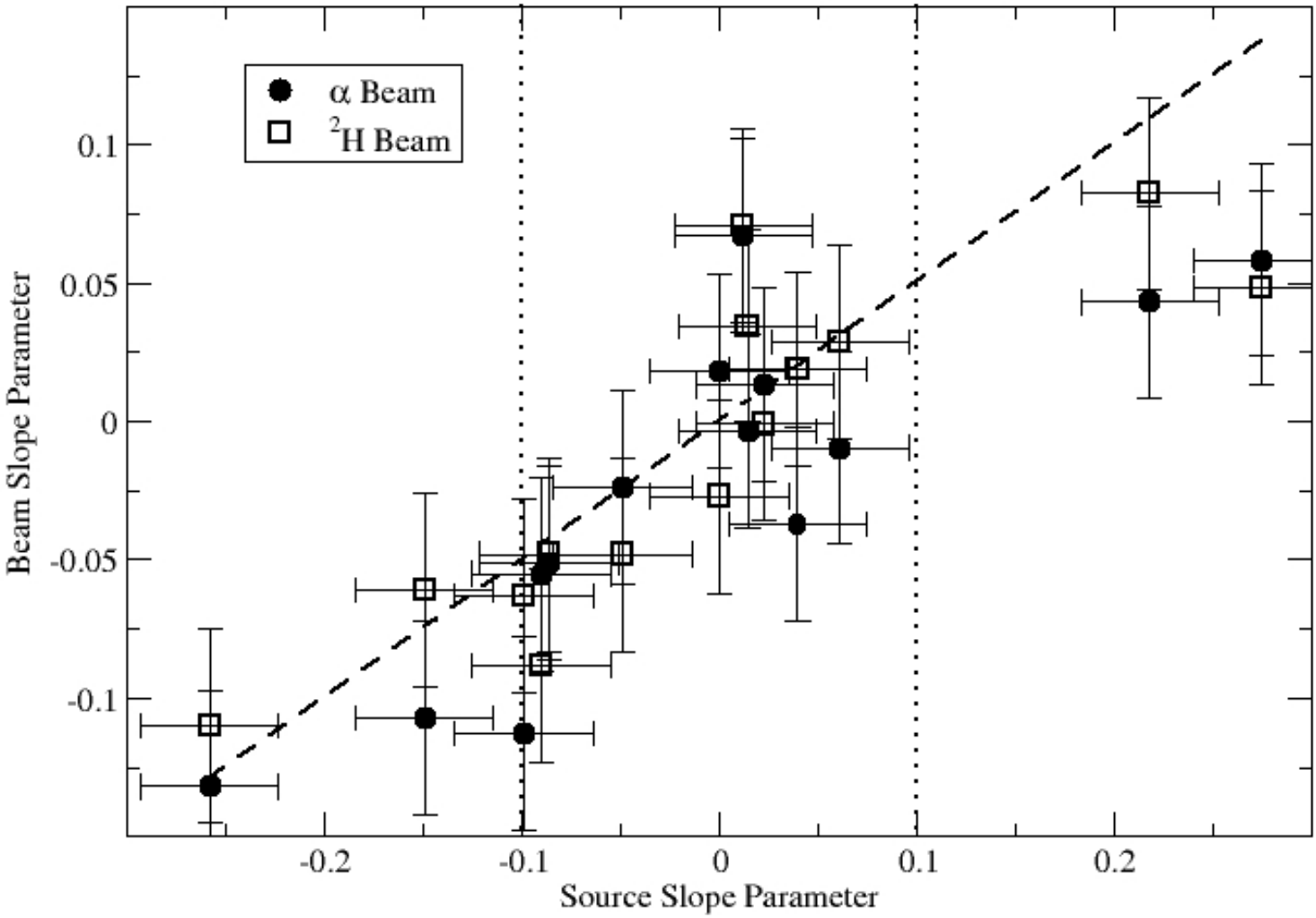

Fig. 7: Panels 7a and 7b shows D_{ij} obtained for the alpha beam using crystals #4 and #6 as in Figure 3 and 5. The corresponding plots for the deuteron beam are shown in Panels 7c and 7d, respectively. The standard deviation of D_{ij}, i.e. $\sqrt{\langle D_{ij}^2 \rangle}$ is also given.

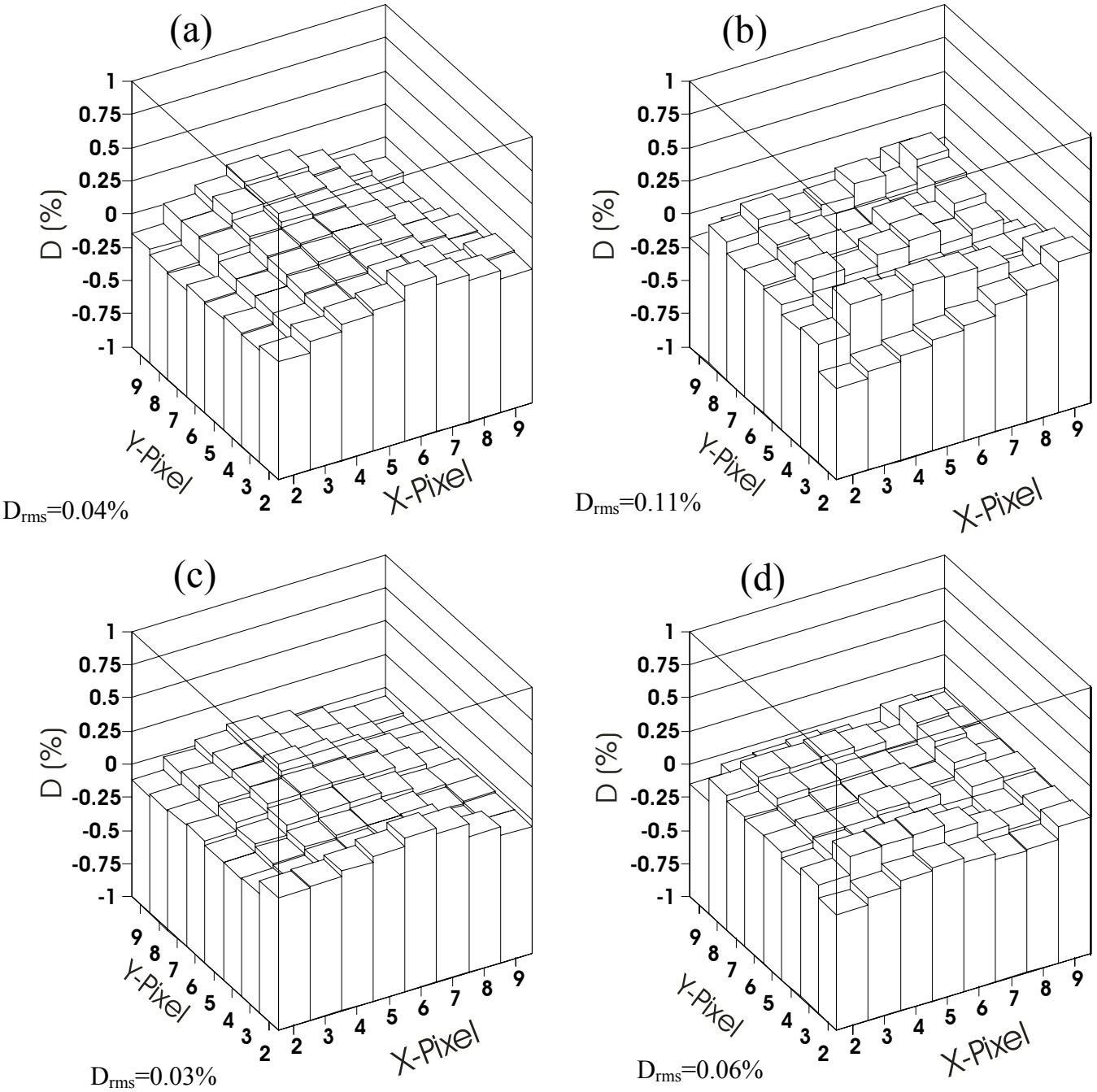

D_{rms}=0.04%

D_{rms}=0.11%

D_{rms}=0.03%

D_{rms}=0.06%

Fig. 8: Left panels: CsI(Tl) crystal #4 with large non-uniformity. Right panels: CsI(Tl) crystal #6 with small non-uniformity. Bottom panels: Results for 110 MeV deuterons. Top panels: Results for 220 MeV alpha particles. In all panels, the dotted lines are the uncorrected energy spectra. The dashed lines are the spectra corrected with the linear correction for the light output non-uniformities. The solid lines are spectra for particles that enter into one randomly chosen pixel in the detectors. The dot-dash line is the crystal spectra corrected using the smoothing algorithm described in the text.

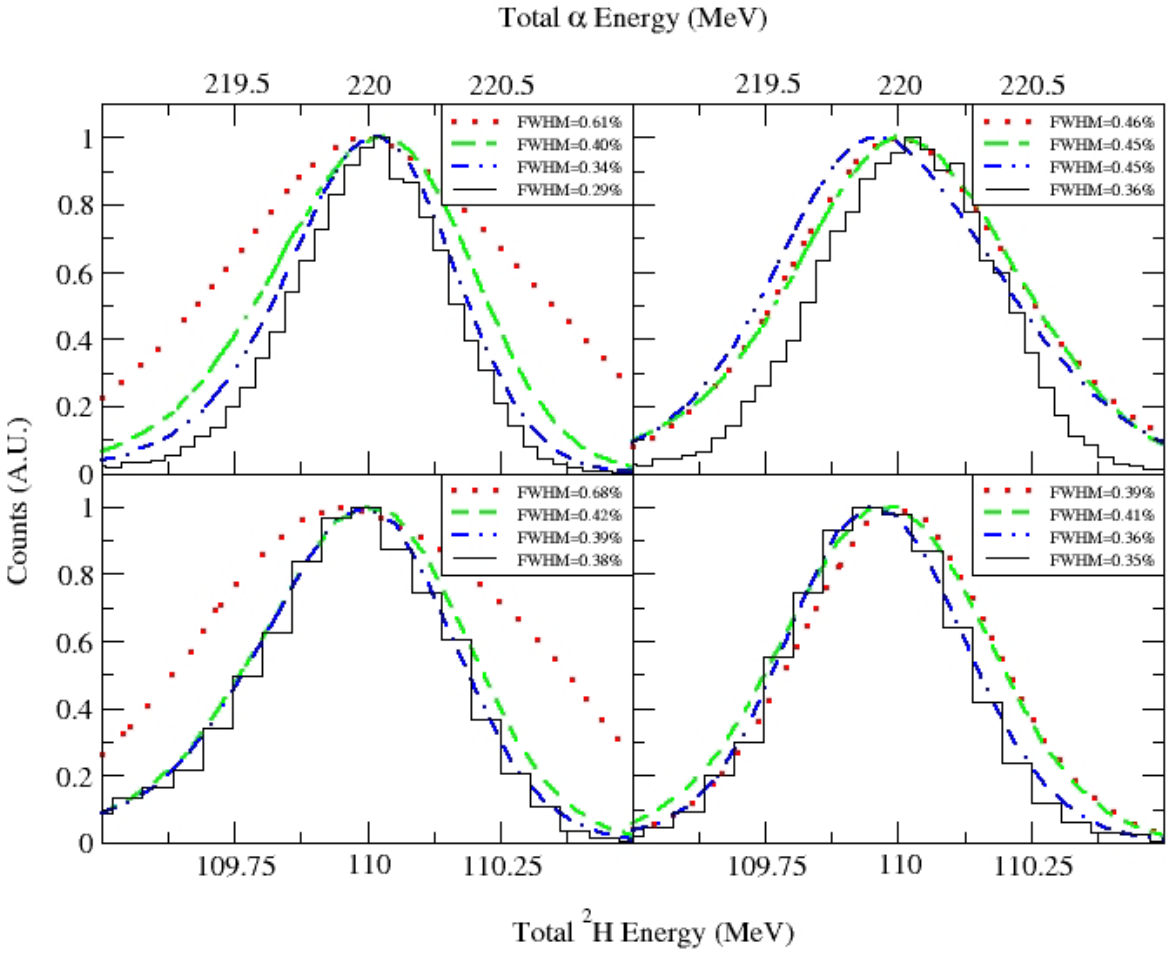

Fig. 9: Non-uniformity values S_{ij} (in) for HiRA crystals #8 (left side) and #9 (right side) for the indicated beam particles from the CCF of the NSCL. Each pixel is separated in both x and y directions from its neighbor by 2 mm. The standard deviation of S_{ij}, i.e. $\sqrt{\langle S_{ij}^2 \rangle}$ is also given.

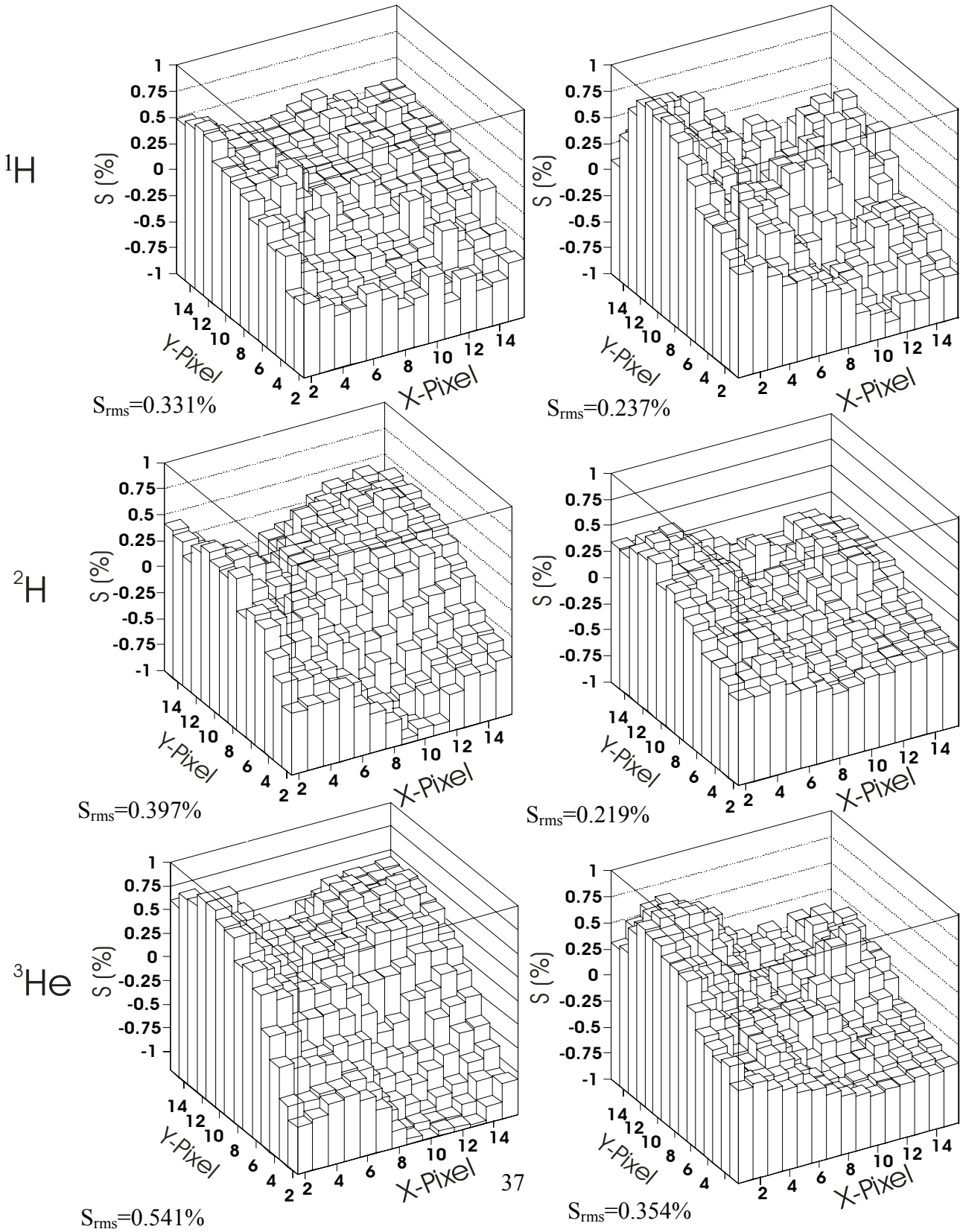

Fig. 10: Non-uniformity values S_{ij} (in) for HiRA crystals #8 (left side) and #9 (right side) for ^{6}Li and ^{7}Be fragmentation beams from the CCF of the NSCL. The standard deviation of S_{ij}, i.e. $\sqrt{\langle S_{ij}^2 \rangle}$ is also given.

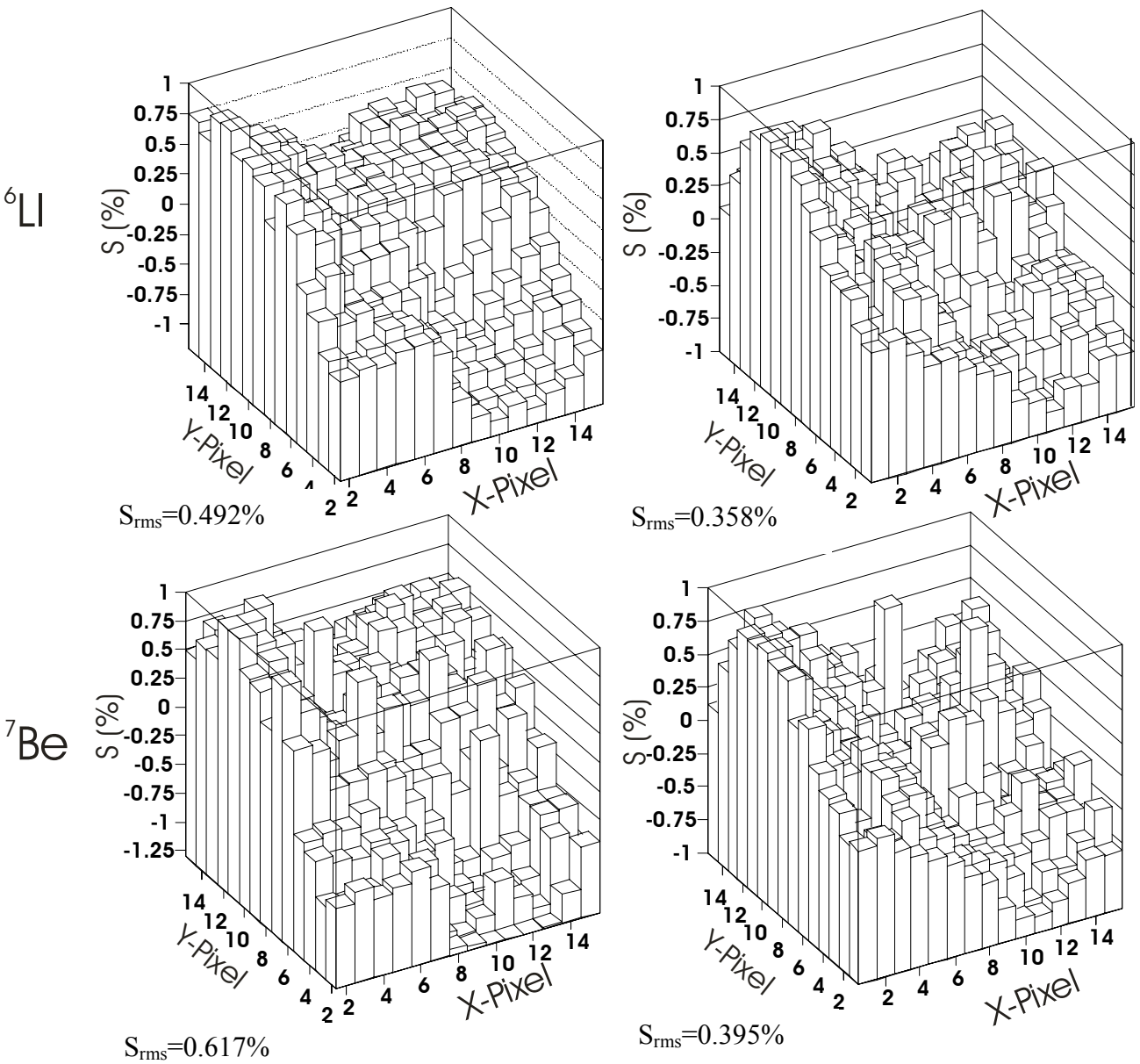

Fig. 11: Smoothed non-uniformity values SM_{ij} in crystals #8 (left side) and #9 (right side) for protons, deuterons, and ^{3}He's measured in the HiRA beam test. The rms values of the smoothed distributions are also shown.

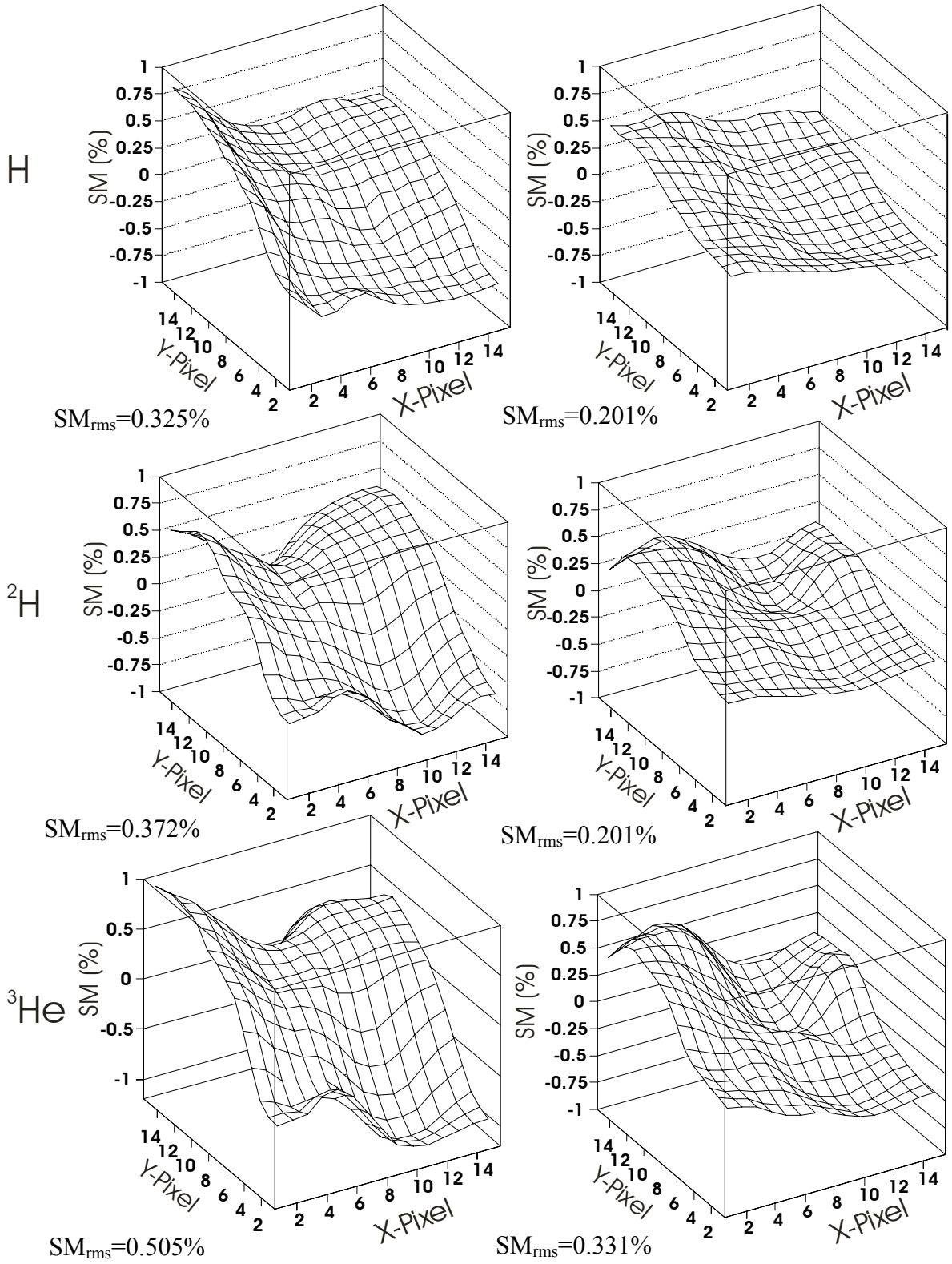

Fig. 12: Smoothed non-uniformity values SM_{ij} for crystals #8 (left side) and #9 (right side) for ^{6}Li and ^{7}Be beams measured in the HiRA beam test. The rms values of the smoothed distributions are also shown.

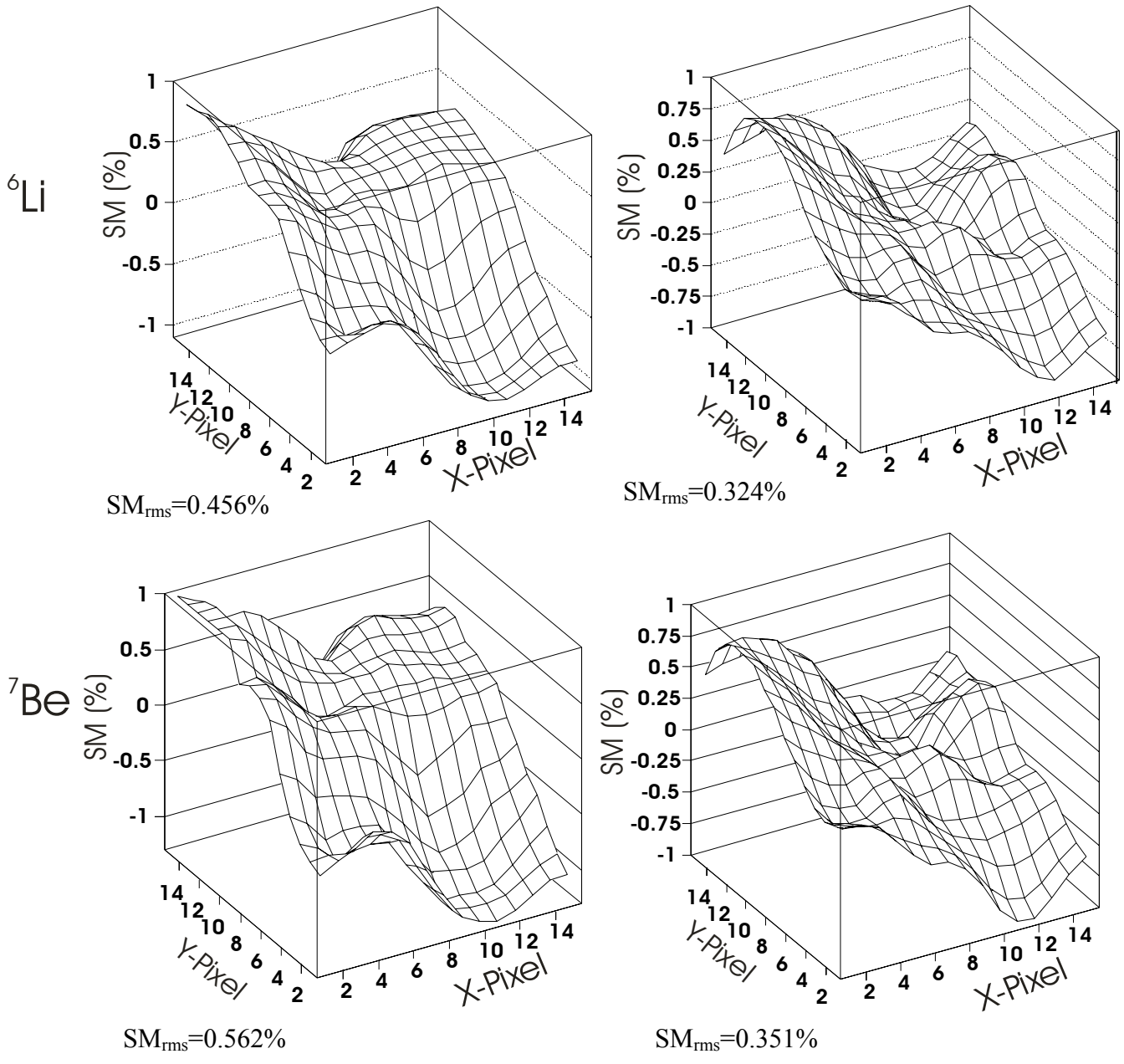

Fig. 13: The smoothed distributions for ^{6}Li (in red) along with scaled deuteron non-uniformities (in black) for crystals #8 (left) and #9 (right). The rms values of the smoothed distributions are also shown.

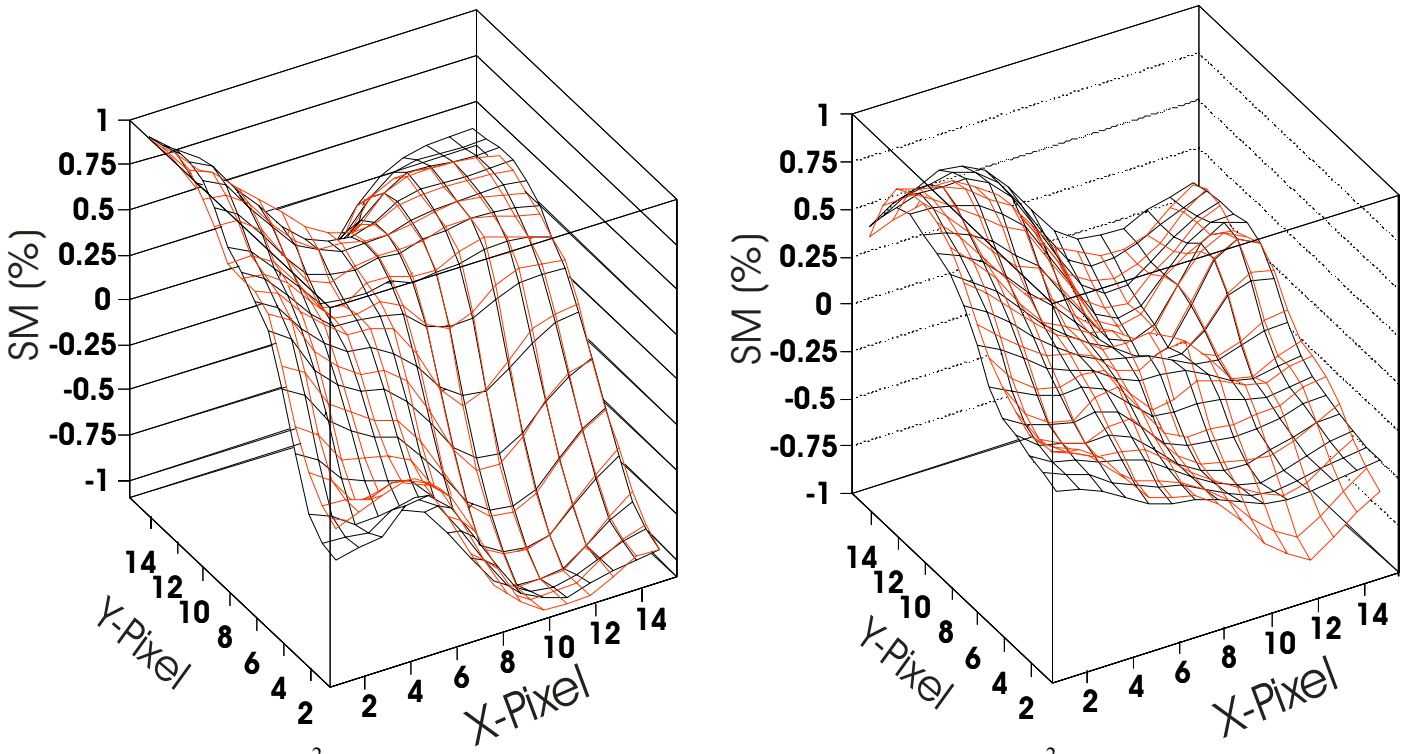

SM_{rms}=0.457% - ^{2}H

SM_{rms}=0.456% - ^{6}Li

SM_{rms}=0.345% - ^{2}H

SM_{rms}=0.324% - ^{6}Li

Fig. 14: The smoothed distributions for deuterons (in black) along with scaled ^{4}He non-uniformities (in red) for crystals #4 (left) and #6 (right). The rms values of the smoothed distributions are also shown.

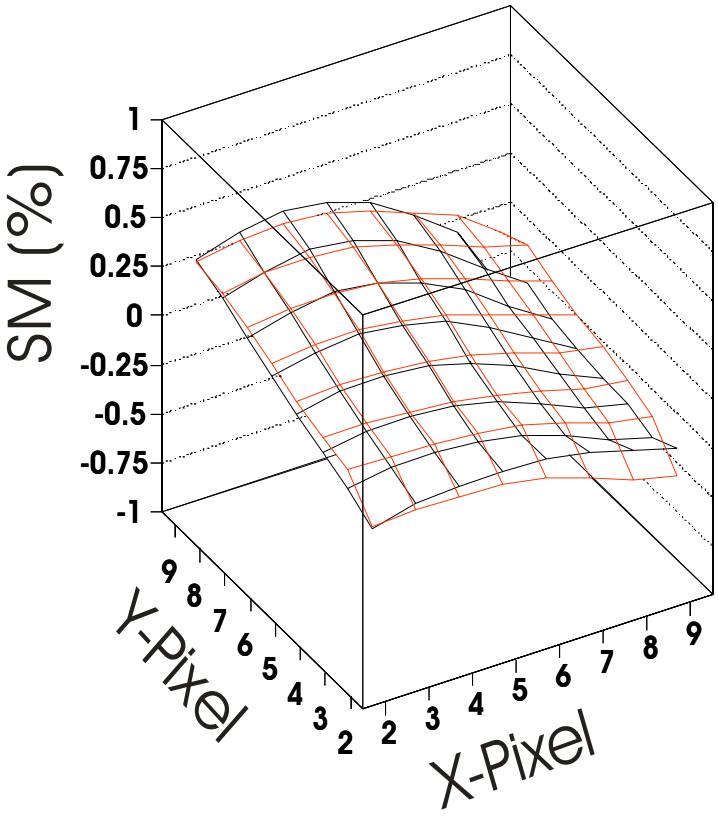

SM_{rms}=0.202% - ^{2}H

SM_{rms}=0.182% - ^{4}He

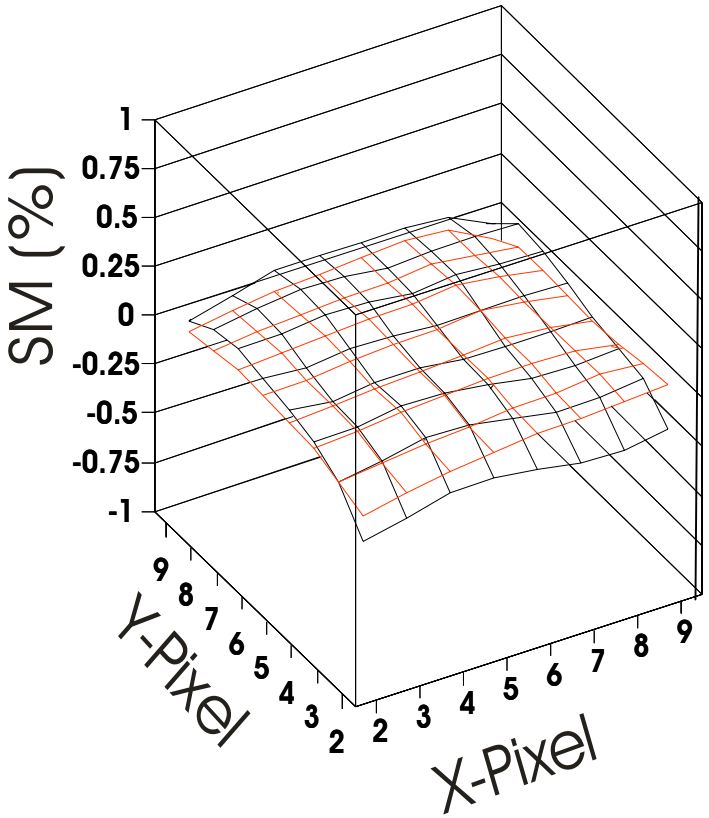

SM_{rms}=0.099% - ^{2}H

SM_{rms}=0.036% - ^{4}He

Fig. 15: Scaling factor α, which describes the non-uniformity of specific isotopes with respect to that for ^{6}Li at E/A=26 MeV for various particles and energies. By construction, we have a value of α=1 at AZ^2/E=0.34 corresponding to the ^{6}Li fragmentation beam. The line is the fit to the non-linear term in Eq. 10.

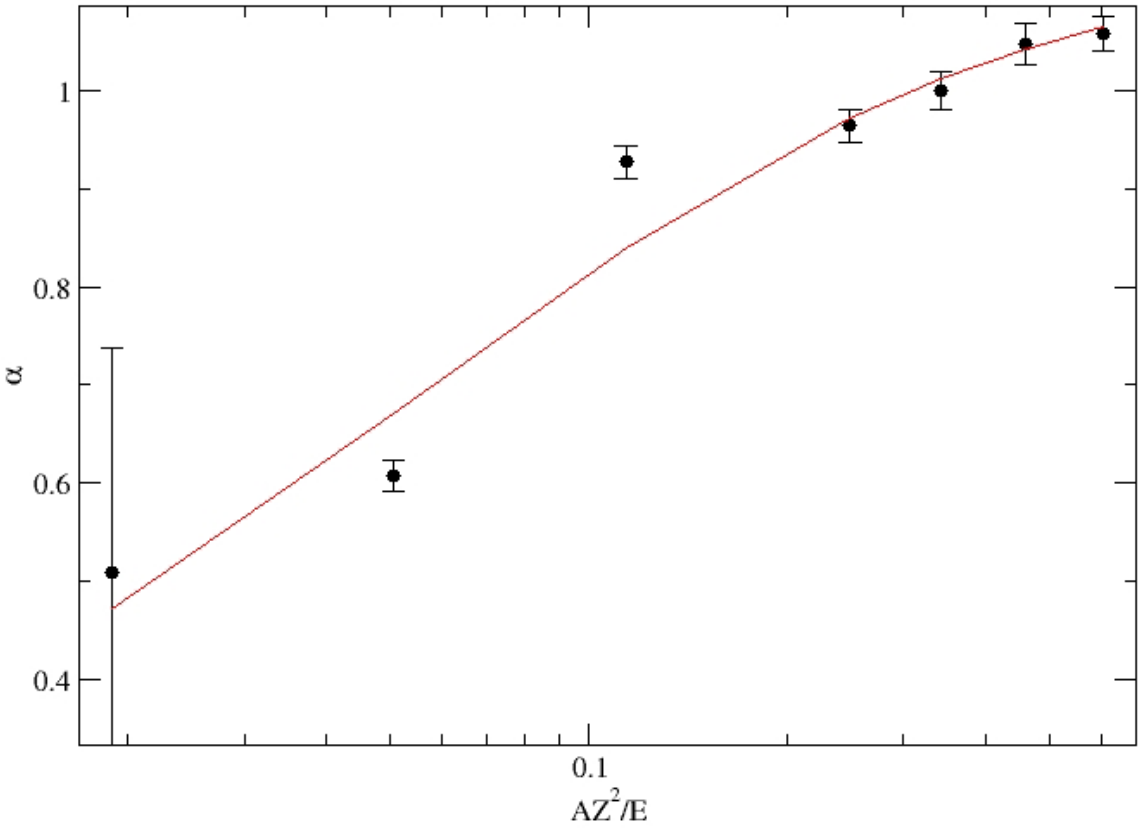

Fig. 16: Residual non-uniformity $D'_{ij}=S_{ij}-SM_{ij}$ for protons (top), deuterons (middle), and ^{3}He (bottom) particles on crystals #8 (left) and #9 (right). The rms values of the corrected distributions are also shown. The large residual non-uniformities around X-Pixel=14 and Y-Pixel=2 are due to low statistics of the scan.

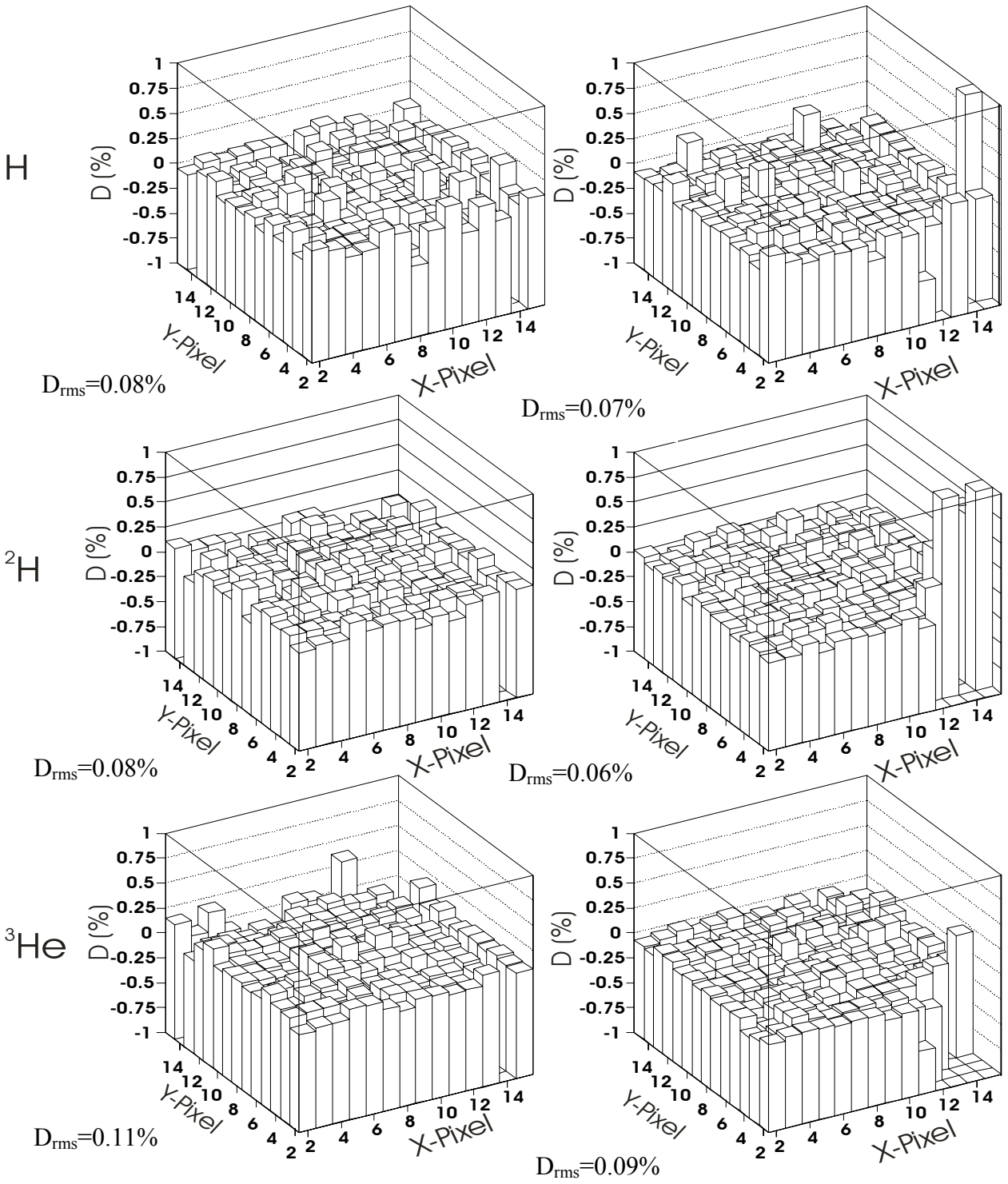

Fig. 17: Residual non-uniformity $D'_{ij}=S_{ij}-SM_{ij}$ for ^{6}Li (top) and ^{7}Be (bottom) using crystals #8 (left) and #9 (right). The rms values of the corrected distributions are also shown.